Model-based fault detection of hybrid fuel cell and photovoltaic direct current power sources

Liyan Zhang [a,*], Alex Q. Huang [b]

[a] School of Automation, Wuhan University of Technology, Wuhan, Hubei Province 430070, China
[b] Department of Electrical and Computer Engineering, North Carolina State University, Raleigh, NC 27606, USA

ARTICLE INFO

ABSTRACT

Hybrid DC power sources which consist of fuel cells, photovoltaic and lithium-ion batteries provide clean, high efficiency power supply. This hybrid DC power sources can be used in many applications. In this work, a model-based fault detection methodology for this hybrid DC power sources is presented. Firstly, the dynamic models of fuel cells, photovoltaic and lithium-ion batteries are built. The state space model of hybrid DC power sources is obtained by linearizing these dynamic models in operation points. Based on this state space model the fault detection methodology is proposed. Simulation results show that model-based fault detection methodology can find the fault on line, improve the generation time and avoid permanent damage to the equipment.

1. Introduction

Currently, most of the energy demand in the world is met by fossil and nuclear power plants. A small part is drawn from renewable energy technologies such as wind, solar, fuel cell, biomass and geothermal energy. Solar energy, fuel cells and wind energy have experienced a remarkably rapid growth in the past 10 years because they are pollution-free power sources. Additionally, they generate power near the load centers, which eliminates the need to run high-voltage transmission lines through rural and urban landscapes. Hybrid DC power sources which consist of fuel cells (FC), photovoltaic (PV) and lithium-ion batteries provide clean, high efficiency power supply. This hybrid DC power sources can be used in many applications such as home power supply, electrical car and satellite power systems. But the structure of hybrid DC power sources is complex and vulnerable to faults. For examples, fuel cells have faults in the air-reaction blower, the refrigeration system, hydrogen pressure and increase of fuel crossover [1,2]. The energy losses of PV system may be resulted from four different fault categories: sustained zero efficiency faults; brief zero efficiency faults; shading; and non-zero efficiency non-shading faults [3]. So it is necessary to study fault detection and diagnosis of this hybrid DC power sources.

Fault detection is a subfield of control engineering which concerns itself with monitoring a system, identifying when a fault has occurred and pinpoint the type of fault and its loca-

tion. A fault is defined as an unexpected change in a system with component malfunction or variation in operating condition. Faults in a dynamic system can take many forms, such as actuator faults, sensor faults and abrupt changes of some parameters. The representative fault detection approaches are model free method, knowledge-based method and model-based method. The model-based fault detection approaches include parity space-based approach [4], eigenstructure assignment-based approach [5], parameter identification-based approach [6] and observer-based approach. Among these methods, observer-based fault detection is one of the most effective methods and has obtained much more attention.

In this paper, a model based fault detection method is proposed to execute on-line fault diagnosis of hybrid DC power sources. The structure of this paper is the following: in Section 2, the models of the hybrid DC power sources were built. In Section 3, the proposed model-based fault diagnosis methodology was described. In Section 4, the hybrid DC power sources system is used to illustrate the proposed fault diagnosis methodology with the fault scenarios that can appear. Finally, in Section 5, conclusions are drawn, based on the results from the numerical analyses in Section 4.

2. Model of hybrid DC power sources

2.1. The structure of hybrid DC power sources

The hybrid DC power system consists of a photovoltaic system, a PEM fuel cell power source, and a lithium-ion battery, which are connected to the same DC voltage bus through appropriate DC/DC

* Corresponding author. Tel.: +86 13018091886; fax: +86 2787859589.
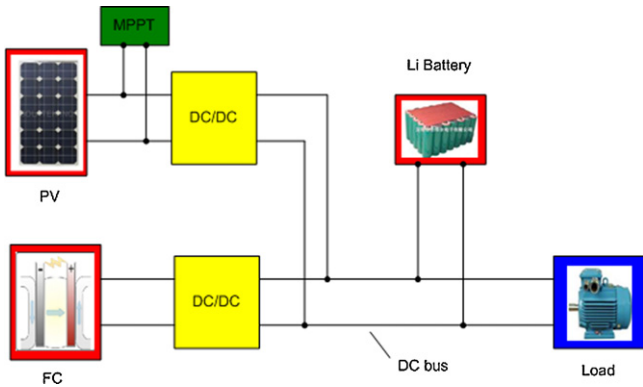E-mail address: zlywhut@whut.edu.cn (L. Zhang).

Fig. 1. Structure of hybrid power sources.

power converters and controller. Fig. 1 illustrates the structure of the proposed hybrid DC power system. There are two main power sources: PV and FC. When the supplies of FC and PV excess the load demands the lithium-ion battery is a power source. In the operation of hybrid DC power sources the PV provides as much power as possible to the load. In order to operate in maximum power point, a maximum power point tracker (MPPT) controller must be installed in PV system. The voltage of DC bus is 288 V and the voltage of PV system is varied between 10 V and 100 V, it is necessary to insert a DC/DC converter between the PV system and DC bus. The FC is to supply the rest power of load. A DC/DC converter is also installed between the FC and DC bus. The lithium-ion battery supplies transient power to peak load demands or absorbs transient power from the main sources. The currents and voltages of the PV panel, the fuel cell, and the lithium-ion battery are monitored. The measured voltages and currents are fed into the power management subsystem, which is used to controls the power flowing from each source of energy, and allocates the available power to recharge the battery if possible.

2.2. Model of PEM fuel cell

We build water balance equation by investigating stack voltage model, water distribution of membrane and water transport process in cathode and anode. In this paper direct injection of water into cathode is used for humidification. The following equations are stack voltage model, water distribution of membrane and water balance equation of cathode and anode.

We assume that single fuel cell is symmetrical the stack voltage can be represented by multiplying the voltage of single fuel cell with number of fuel cell.

$$V_{st} = n \cdot V_{fc} \tag{1}$$

The voltage of single fuel cell V_{fc} is calculated as a function of current, cathode pressure, reactant partial pressures, stack temperature and membrane humidity. There are a lot of voltage model in the literature, we adopt the semi-empirical model in this paper [7]:

$$V_{fc} = E_0 - V_{act} - V_{ohm} - V_{conc} \tag{2}$$

E_0 is the thermodynamic potential of the cell representing its reversible voltage:

$$E_0 = 1.229 - 0.85 \times 10^{-3}(T - 298.15)$$
$$+ 4.3085 \times 10^{-5}T \left[\ln(p_{H_2}) + 0.5 \ln(p_{O_2}) \right] \tag{3}$$

where T is operating temperature, P_{H_2} is the hydrogen pressure and P_{O_2} is the oxygen pressure.

Activation voltage loss V_{act} is the voltage drop due to the activation of the anode and the cathode:

$$V_{act} = V_0 + V_a(1 - e^{-c_1 i}) \tag{4}$$

where c_1 is parameter [7,8], V_a and V_0 can be calculated as follows:

$$V_0 = 0.279 - 8.5 \times 10^{-4}(T - 298.15) + 4.308 \times 10^{-5}T$$
$$\times \left[\ln\left(\frac{p_{ca} - p_{sat}}{1.01325}\right) + \frac{1}{2}\ln\left(\frac{0.01173(p_{ca} - p_{sat})}{1.01325}\right) \right] \tag{5}$$

$$V_a = (-1.618 \times 10^{-5}T + 1.618 \times 10^{-2})\left(\frac{p_{O_2}}{0.1173} + p_{sat}\right)^2$$
$$+ (1.8 \times 10^{-4}T - 0.166)\left(\frac{p_{O_2}}{0.1173} + p_{sat}\right)$$
$$+ (-5.8 \times 10^{-4}T + 0.5736) \tag{6}$$

V_{ohm} is the ohmic voltage drop associated with the conduction of protons through the electrolyte, and of electrons through the internal electronic resistance and calculated as follows:

$$V_{ohm} = i \cdot R_{ohm} = i \cdot \frac{t_m}{\sigma_m} \tag{7}$$

where t_m is the thickness of membrane, σ_m is the membrane conductivity and calculated as follows:

$$\sigma_m = b_1 \exp\left(b_2\left(\frac{1}{303} - \frac{1}{T}\right)\right) \tag{8}$$

in which b_2 constant [9], b_1 function of water content of membrane λ_m.

V_{conc} is the concentration voltage loss resulted from the drop in concentration of the reactants as they are consumed in the reaction:

$$V_{conc} = i\left(\frac{c_2 i}{i_{max}}\right)^{c_3} \tag{9}$$

where c_2, c_3 and i_{max} are constants [8] and depend on stack temperature and pressure of reactants.

The governing equation for hydrogen and water in the anode can be written as:

$$\frac{dm_{H_2}}{dt} = W_{H_2,in} - W_{H_2,out} - W_{H_2,rec} \tag{10}$$

$$\frac{dm_{w,an}}{dt} = W_{w,an,in} - W_{w,an,out} - W_{w,mbr} \tag{11}$$

The hydrogen and water flowing to the anode are calculated by

$$W_{H_2,in} = (1 - \alpha)W_{an,in} \tag{12}$$

$$W_{w,an,in} = \alpha W_{an,in} \tag{13}$$

where α is inlet flow humidity ratio in anode.

The outlet hydrogen and vapor mass flow rate are calculated by the following equations:

$$W_{H_2,an,out} = \frac{1}{1 + \omega_{an,out}}W_{an,out} \tag{14}$$

$$W_{w,an,out} = \frac{\omega_{an,out}}{1 + \omega_{an,out}}W_{an,out} \tag{15}$$

$$\omega_{an,out} = \frac{M_v}{M_{H_2}} \cdot \frac{m_{H_2}R_{H_2}}{m_{v,an}R_{H_2}} \tag{16}$$

Inside the cathode there are three elements: oxygen, nitrogen and water. The balance equation for the mass of these elements can be written as:

$$\frac{dm_{O_2}}{dt} = W_{O_2,in} - W_{O_2,out} - W_{O_2,rec} \tag{17}$$

$$\frac{dm_{N_2}}{dt} = W_{N_2,in} - W_{N_2,out} \tag{18}$$

$$\frac{dm_{\omega,ca}}{dt} = W_{w,ca,in} - W_{w,ca,out} + W_{w,gen} + W_{w,mbr} + W_{inj} \qquad (19)$$

where $W_{O_2,in}$ is the mass flow rate of oxygen gas entering the cathode; $W_{O_2,out}$ is the mass flow rate of oxygen gas leaving the cathode; $W_{O_2,rec}$ is the mass flow rate of oxygen reacted; $W_{N_2,in}$ is the mass flow rate of nitrogen gas entering the cathode; $W_{N_2,out}$ is the mass flow rate of nitrogen gas leaving the cathode; $W_{w,ca,in}$ is the mass flow rate of vapor entering the cathode; $W_{w,ca,out}$ is the mass flow rate of vapor leaving the cathode; $W_{w,gen}$ is the mass flow rate of vapor generated in the fuel cell reaction; $W_{w,inj}$ is the mass flow rate of injected water from humidifier; $W_{w,mem}$ is the mass flow rate of water transfer across the membrane.

Inlet mass of oxygen, nitrogen and vapor is related to mass flow rate and humidity of inlet air:

$$W_{O_2,in} = y_{O_2}\frac{1}{(1+\Omega_{atm})W_{ca,in}} \qquad (20)$$

$$W_{N_2,in} = y_{N_2}\frac{1}{(1+\Omega_{atm})W_{ca,in}} \qquad (21)$$

$$W_{w,ca,in} = \frac{\Omega_{atm}}{(1+\Omega_{atm})W_{ca,in}} \qquad (22)$$

where Ω_{atm} is the humidity ratio of air, y_{O_2} and y_{N_2} are oxygen mole fraction and nitrogen mole fraction of dry air.

$$y_{O_2} = x_{O_2}\frac{MO_2}{M_a^{atm}} \qquad (23)$$

$$y_{N_2} = (1-x_{O_2})\frac{M_{N_2}}{M_a^{atm}} \qquad (24)$$

x_{O_2} is volume content of oxygen in dry air.

$$M_a^{atm} = x_{O_2}MO_2 + (1-x_{O_2})M_{N_2} \qquad (25)$$

The calculations of $W_{O_2,out}$, $W_{N_2,out}$, $W_{w,ca,out}$, $W_{w,mem}$ can find in Ref. [8].

The rate of oxygen consumed in the reaction and water generated in the reaction is calculated by

$$W_{O_2,rct} = \frac{M_{O_2}(nI_{st})}{4F} \qquad (26)$$

$$W_{H_2,rct} = \frac{M_{H_2}(nI_{st})}{2F} \qquad (27)$$

$$W_{w,gen} = \frac{M_{H_2O}(nI_{st})}{2F} \qquad (28)$$

According to Ref. [8], $W_{ca,out}$ is outlet gas flow rate and calculated as follows:

$$W_{ca,out} = k_{ca,out}(P_{ca} - P_{atm}) \qquad (29)$$

where $k_{ca,out}$ is an orifice constant, P_{ca} is gas pressure of cathode and include the partial pressure of oxygen P_{O_2}, the partial pressure of nitrogen P_{N_2} and the partial pressure of vapor $P_{v,ca}$:

$$P_{ca} = P_{O_2} + P_{N_2} + P_{v,ca} \qquad (30)$$

$$P_{O_2} = \frac{m_{O_2}R_{O_2}T}{V_{ca}} \qquad (31)$$

$$P_{N_2} = \frac{m_{N_2}R_{N_2}T}{V_{ca}} \qquad (32)$$

$$P_{v,ca} = \frac{m_{v,ca}R_v T}{V_{ca}} \qquad (33)$$

where R_{O_2}, R_{N_2} and R_v are gas constants of oxygen, nitrogen and vapor, respectively.

According to the above nonlinear model, there are five state variables $x = [m_{H_2}, m_{w,an}, m_{O_2}, m_{N_2}, m_{w,ca}]$. The parameters used in this model are given in Table 1. Most of the parameters are based

Table 1
Model parameters of PEM fuel cell.

Symbol	Variable	Value
R_{H_2}	Hydrogen gas constant	$4124.3\,\mathrm{J\,(kg\,K)^{-1}}$
R_{N_2}	Nitrogen gas constant	$296.8\,\mathrm{J\,(kg\,K)^{-1}}$
R_{O_2}	Oxygen gas constant	$259.8\,\mathrm{J\,(kg\,K)^{-1}}$
R_v	Vapor gas constant	$461.5\,\mathrm{J\,(kg\,K)^{-1}}$
M_{H_2}	Hydrogen molar mass	$2.016\times10^{-3}\,\mathrm{kg\,mol^{-1}}$
M_{O_2}	Oxygen molar mass	$32\times10^{-3}\,\mathrm{kg\,mol^{-1}}$
M_{N_2}	Nitrogen molar mass	$28\times10^{-3}\,\mathrm{kg\,mol^{-1}}$
R_a	Air gas constant	$286.9\,\mathrm{J\,(kg\,K)^{-1}}$
P_{atm}	Atmospheric pressure	101.325 kPa
n	Number of cells in FC stack	381
A_{fc}	Fuel cell active area	$280\,\mathrm{cm^2}$
V_{an}	Anode volume	$0.005\,\mathrm{m^3}$
V_{ca}	Cathode volume	$0.01\,\mathrm{m^3}$
F	Faraday number	96485
φ_{atm}	The humidity ratio of air	0.5
c_1	Constant	10
b_2	Constant	350
c_3	Constant	2
i_{max}	Maximum current density	2.2

on the 75 kW stacks used in the FORD P2000 fuel cell prototype vehicle [8,9]. This stack consists of 381 single fuel cells, the membrane of single fuel cell is Nafion 117. We linearize the FC system at the nominal operating point with stack current as 200 A and stack temperature as 338 K, we can get state space equation of fuel cell system:

$$\begin{aligned}\dot{x} &= A_1 x + B_1 u \\ y &= C_1 x + D_1 u\end{aligned} \qquad (34)$$

where $x = [m_{H_2}, m_{w,an}, m_{O_2}, m_{N_2}, m_{w,ca}]$ is state variable, $u = [W_{inj}, W_{CP}]$ is control input variable, $y = [V_{st}, W_{ca,out}]$ is output variable.

2.3. Model of PV system

The current–voltage relationship at a fixed cell temperature and solar radiation is expressed as follows:

$$I = I_L - I_o[e^{(V+IR_s)/a} - 1] - \frac{V+IR_s}{R_{sh}} \qquad (35)$$

where I_L is photo current, I_o is the diode reverse saturation current, R_s is the series resistance, R_{sh} is the shunt resistance, and a is the modified ideality factor.

The parameters in Eq. (35) corresponding to operation at standard rating condition (SRC) are designed: a_{ref}, $I_{L,ref}$, $I_{o,ref}$. To determine the values of these parameters [10], the three known I–V pairs at SRC are substituted into Eq. (35).

For short circuit current: $I = I_{sc,ref}$, $V = 0$

$$I_{sc,ref} = I_{L,ref} - I_{o,ref}\left[e^{I_{sc,ref}R_s/a_{ref}} - 1\right] - \frac{I_{sc,ref}R_s}{R_{sh}} \qquad (36)$$

For open circuit voltage: $I = 0$, $V = V_{oc,ref}$.

$$0 = I_{L,ref} - I_{o,ref}\left[e^{V_{oc,ref}/a_{ref}} - 1\right] - \frac{V_{oc,ref}}{R_{sh}} \qquad (37)$$

At the maximum power point: $I = I_{smp,ref}$, $V = V_{smp,ref}$.

$$I_{mp,ref} = I_{L,ref} - I_{o,ref}\left[e^{(V_{mp,ref}+I_{mp,ref}R_s)/a_{ref}} - 1\right]$$
$$- \frac{V_{mp,ref} + I_{mp,ref}R_s}{R_{sh}} \qquad (38)$$

Then the modified ideality factor a is a linear function of cell temperature:

$$a = \frac{T_c a_{ref}}{T_{c,ref}} \qquad (39)$$

Table 2
PV system's model parameters.

Symbol	Variable	Value
R_s	Series resistance	$0.969\,\Omega$
R_{sh}	Shunt resistance	$199\,\Omega$
S_{ref}	Total absorbed irradiance at SRC	$1000\,\mathrm{Wm^{-2}}$
$I_{sc,ref}$	Short circuit current at SRC	$4.37\,\mathrm{A}$
$V_{oc,ref}$	Open circuit voltage at SRC	$42.93\,\mathrm{V}$
$T_{c,ref}$	Cell temperature at SRC	$298\,\mathrm{K}$
k	Boltzmann's constant	$1.3805\mathrm{e}{-23}\,\mathrm{J\,K^{-1}}$
q	Electron charge	$1.6\mathrm{e}{-19}\,\mathrm{C}$

where $T_{c,ref}$ is the cell temperature for reference condition and T_c is the cell temperature.

The diode reverse saturation current I_o is calculated as follow:

$$I_o = \left(\frac{T_c}{T_{c,ref}}\right)^3 \exp\left[\frac{1}{k}\cdot\left(\left.\frac{E_g}{T}\right|_{T_{ref}} - \left.\frac{E_g}{T}\right|_{T_c}\right)\right] \tag{40}$$

where k is Boltzmann's constant and E_g is the material band gap.

E_g can be calculated as follows:

$$E_g = E_{g,T_{ref}}\left[1 - 0.0002677(T - T_{ref})\right] \tag{41}$$

where $E_{g,T_{ref}} = 1.121$ eV for silicon cells and $E_{g,T_{ref}} = 1.6$ eV for the triple junction amorphous cell.

Photo current I_L is calculated as follow:

$$I_L = \frac{S}{S_{ref}} \times (I_{L,ref} + \alpha_{Isc}(T_c - T_{c,ref})) \tag{42}$$

where S is total absorbed irradiance ($\mathrm{Wm^{-2}}$), α_{Isc} is temperature coefficient for short circuit current ($\mathrm{AK^{-1}}$). S_{ref} is total absorbed irradiance at SRC ($\mathrm{Wm^{-2}}$).

PV system's model parameters in this paper are listed in Table 2. The V–I curve of PV's single cell is shown in Fig. 2. The curve can be divided into three zones: current zone, maximal power zone and voltage zone. When $0 \leq V_{pv} \leq V_1$ the V–I curve is under current zone, the state space equation is $I_{pv} = I_{sc} + \alpha_1 V_{pv}$. When $V_1 \leq V_{pv} \leq V_2$ the V–I curve is under maximal power zone, the state space equation is $I_{pv} = \alpha_1 V_{pv} - \alpha_2 V_{mp} + I_{mp}$. When $V_2 \leq V_{pv} \leq V_{oc}$ the V–I curve is under voltage zone, the state space equation is $I_{pv} = \alpha_3 V_{pv} - \alpha_3 V_{oc}$. The parameter $\alpha_1, \alpha_2, \alpha_3, V_1, V_2$ can be calculated from Eqs. (34) to (42).

State space equation can be obtained by linearizing the PV system:

$$\begin{aligned} \dot{x} &= A_2 x + B_2 u \\ y &= C_2 x + D_2 u \end{aligned} \tag{43}$$

where state variable is I_{pv}, control variable is V_{pv} and output variable is I_{pv}.
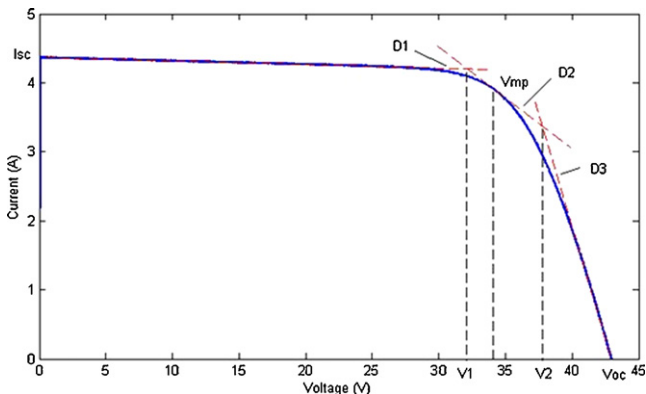
Fig. 2. V–I curve of PV's single cell.

Table 3
Model parameters of lithium-ion battery.

Symbol	Variable	Value
R_1	Resistance	40×10^{-3}
R_2	Resistance	110×10^{-3}
C	Capacitance	$4\,\mathrm{F}$
c_p	Specific heat	$925\,\mathrm{J\,(kg\,K)^{-1}}$
m	Battery mass	$0.041\,\mathrm{kg}$
A	Battery external surface area	$4.3 \times 10^{-3}\,\mathrm{m^2}$
T_a	Ambient temperature	$23\,^\circ\mathrm{C}$

2.4. Model of lithium-ion battery

The equilibrium potential of the lithium-ion battery depends on the temperature and the amount of active material available in the electrodes, which can be specified in terms of state of discharge (SOD). The discharge capacity of the battery depends on the discharge rate and the temperature.

The expression for the potential, the terminal voltage and the SOD [11] can be given by

$$E[i_b(t), T_b(t), t] = v[i_b(t), T_b(t), t] - R_{int}i_b(t) \tag{44}$$

$$V[i_b(t), T_b(t), t] = \sum_{k=0}^{n} c_k \cdot SOD^k[i_b(t), T_b(t), t] + \Delta E(T_b) \tag{45}$$

$$SOD[i_b(t), T_b(t), t] = \frac{1}{Q_t}\int_0^t \alpha[i_b(t)]\beta[T_b(t)]\cdot i_b(t)dt \tag{46}$$

According to data from a Sony18650 lithium ion battery, $\alpha[T(t)]$ and $\beta[T(t)]$ can be calculated as follows:

$$\alpha[i_b(t)] = \begin{cases} 1.05 & \text{if } i_b(t) > 2.8\,\mathrm{A} \\ 1.01 + 1.04/1.4*(i_b(t)-1.4) & \text{if } 1.4 < i_b(t) \leq 2.8\,\mathrm{A} \\ 1 + 0.01/0.7*(i_b(t)-0.7) & \text{if } 0.7 < i_b(t) \leq 1.4\,\mathrm{A} \\ 0.96 & \text{if } 0 \leq i_b(t) \leq 0.3\,\mathrm{A} \end{cases} \tag{47}$$

$$\beta[T_b(t)] = \begin{cases} 1.085 - 0.0015(T_b(t)+20) & \text{if } -20\,^\circ\mathrm{C} \leq T_b(t) \leq -10\,^\circ\mathrm{C} \\ 1.075 - 0.0007(T_b(t)+10) & \text{if } -10\,^\circ\mathrm{C} < T_b(t) \leq 0\,^\circ\mathrm{C} \\ 1.063 - 0.00286T_b(t) & \text{if } -0\,^\circ\mathrm{C} < T_b(t) \leq 22\,^\circ\mathrm{C} \\ 1 - 0.001(T_b(t)-22) & \text{if } -22\,^\circ\mathrm{C} \leq T_b(t) \leq 45\,^\circ\mathrm{C} \end{cases} \tag{48}$$

$$\Delta E[T_b(t)] = \begin{cases} -0.46 + 0.012(T_b(t)+20) & \text{if } -20\,^\circ\mathrm{C} \leq T_b(t) \leq -10\,^\circ\mathrm{C} \\ -0.38 + 0.025(T_b(t)+10) & \text{if } -10\,^\circ\mathrm{C} < T_b(t) \leq 0\,^\circ\mathrm{C} \\ 0.13 + 0.0059T_b(t) & \text{if } 0\,^\circ\mathrm{C} < T_b(t) \leq 22\,^\circ\mathrm{C} \\ 0.0104(T_b(t)-22) & \text{if } 22\,^\circ\mathrm{C} \leq T_b(t) \leq 45\,^\circ\mathrm{C} \end{cases} \tag{49}$$

Combining the electrochemical characteristics represented with the equation for the circuit elements and the circuit constraint equation yields the following equation that relates the terminal potential to the terminal current

$$\begin{aligned} i_b(t) = &\frac{1}{R_2} \times [V_b(t) - E[i_b(t), T_b(t), t] - R_1 i_b(t)] \\ &+ C\frac{d}{dt}[V_b(t) - E[i_b(t), T_b(t), t] - R_1 i_b(t)] \end{aligned} \tag{50}$$

The temperature change of the battery is governed by the thermal energy balance [12] described by

$$\begin{aligned} m \cdot c_p \cdot \frac{dT_p(t)}{dt} = &i_b(t)^2 \cdot R_1 + \frac{1}{R_2}[V_b(t) - E[i_b(t), T_b(t), t] - i_b(t)R_1]^2 \\ &- h_c A[T_b(t) - T_a] \end{aligned} \tag{51}$$

Model parameters of lithium-ion battery in this paper are listed in Table 3.

State space equation can be divided into 16 sub-models, where i_b is divided into four zones according to Eq. (47) and T_b is also divided into four zones according to Eq. (48). State space equation

of lithium-ion battery can be obtained by linearizing the nonlinear model of lithium-ion battery,

$$\dot{x} = A_3 x + B_3 u$$
$$y = C_3 x + D_3 u \tag{52}$$

where state variable x is $[i_b, T_b]$, control variable u is V_b and output variable y is i_b.

3. Design of model-based fault diagnosis

The design of a fault detection system requires obviously quick fault detection and isolation (FDI) for adequate decision making. Hence, to preserve the safety of operators and the reliability of processes, the presence of faults must be taken into account during the system control design. During the system operation, faults or failures may affect the sensors, the actuators, or the system components. These faults can occur as additive or multiplicative faults due to a malfunction or equipment aging.

The state space representation of hybrid FC and photovoltaic DC power sources system is as follows:

$$\dot{x} = Ax + Bu$$
$$y = Cx + Du \tag{53}$$

where state variables x are $[m_{H_2}, m_{w,an}, m_{O_2}, m_{N_2}, m_{w,ca}, I_{pv}, i_b, T_b]$, output variables y are $[V_{st}, W_{ca,out}, I_{pv}, i_b]$ and control variable u is $[W_{inj}, W_{cp}, V_{pv}, V_b]$.

After the continuous state space model is converted into discrete state space model, the state space representation of a system that may be affected by actuator or sensor fault [13]:

$$x(k+1) = Ax(k) + Bu(k) + F_a f_a(k)$$
$$y(k) = Cx(k) + F_s f_s(k) \tag{54}$$

where F_a and F_b are assumed to be known matrices, f_a and f_b are the magnitude of the actuator and the sensor faults, respectively.

In the presence of sensor and actuator faults, Eq. (54) can also be represented by the unified general formulation:

$$\begin{cases} x(k+1) = Ax(k) + Bu(k) + F_x f(k) \\ y(k) = Cx(k) + F_y f(k) \end{cases} \tag{55}$$

where $f = [f_a^T \ f_s^T]^T$ is a common representation of sensor's and actuator's faults. The fault vector f in (55) can be split into two parts. The first part contains the "d" faults to be isolated. In the second part, the other faults are gathered in a vector.

The fault magnitude estimation of the corrupted element is extracted directly from the jth unknown input observer which is built to be insensitive to the jth fault ($f^*(k) = 0$). Based on the unknown input observer, the substitution of the state estimation in the faulty description [13] leads to

$$F_d f_d(k) = \hat{x}(k+1) - A\hat{x}(k+1) - Bu(k) \tag{56}$$

In the presence of an actuator fault, F_d is a matrix of full column rank. Thus, the estimation of the fault magnitude $\hat{f}_0(k) = \hat{f}_d(k)$ makes use of the singular-value decomposition (SVD) [14].

Let $F_d = U \begin{bmatrix} R \\ 0 \end{bmatrix} V^T$ be the SVD of F_d. Thus R is a diagonal and nonsingular matrix and U and V are orthonormal matrices.

Using the SVD and substituting it into (56) and results in

$$\bar{\tilde{x}}(k+1) = \bar{A}\bar{\tilde{x}}(k) + \bar{A}\bar{\tilde{u}}(k) + \begin{bmatrix} R \\ 0 \end{bmatrix} V^T f_d(k) \tag{57}$$

where

$$\bar{A} = U^{-1}AU = \begin{bmatrix} \bar{A}_{11}(k) & \bar{A}_{12}(k) \\ \bar{A}_{21}(k) & \bar{A}_{22}(k) \end{bmatrix}$$
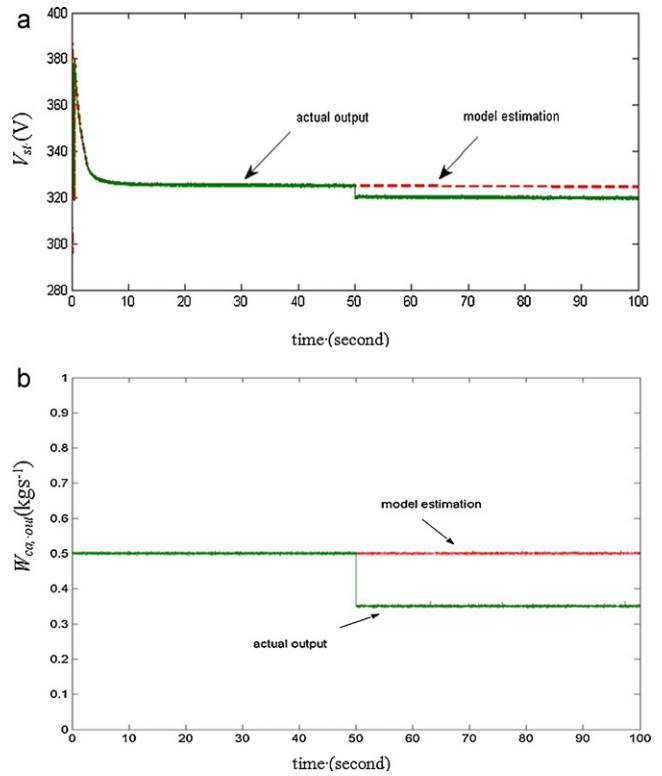

Fig. 3. Comparison of actual output and model estimation when $W_{ca,in}$ is decreased 20%.

$$\bar{B} = U^{-1}B = \begin{bmatrix} \bar{B}_1(k) \\ \bar{B}_2(k) \end{bmatrix}$$

Then the estimation of the actuator fault magnitude is defined as

$$\hat{f}_d(k) = VR^{-1}(\hat{x}_1(k+1) - \bar{A}_{11}\hat{x}_1(k) - \bar{A}_{12}\hat{x}_2(k) - \bar{B}_1 u(k)) \tag{58}$$

For sensor faults, the output equation is broken down and can be written as

$$y(k) = Cx(k) + E_s f_s(k) = \begin{bmatrix} C_1 \\ C_2 \end{bmatrix} x(k) + \begin{bmatrix} F_{s1} \\ F_{s2} \end{bmatrix} f_s(k) \tag{59}$$

The integral error vector z will be affected by the fault as well. The integral error vector can be described as follows:

$$\begin{aligned} z(k+1) &= z(k) + T_s(y_r(k) - y_1(k)) \\ &= z(k) + T_s(y_r(k) - c_1 x(k) - F_{s1} f_s(k)) \end{aligned} \tag{60}$$

The sensor fault magnitude can be estimated as follows:

$$\bar{E}_s \bar{X}_s(k+1) = \bar{A}_s \bar{X}_s(k) + \bar{B}_s \bar{U}(k) + \bar{G}_s y_r(k) \tag{61}$$

where

$$\bar{E}_s = \begin{bmatrix} I_n & 0 & 0 \\ 0 & I_p & 0 \\ 0 & 0 & F_s \end{bmatrix}$$

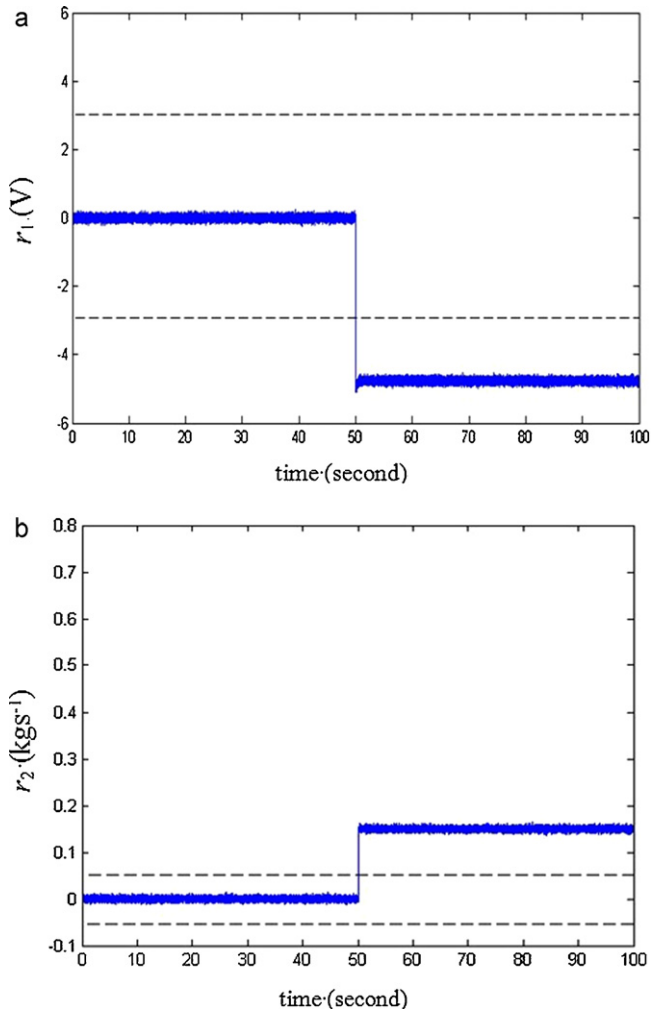$$\bar{X}_s(k) = \begin{bmatrix} x(k) \\ z(k) \\ f_s(k) \end{bmatrix}$$

$$\bar{A}_s = A$$

Fig. 4. Time evolution of the residual when $W_{ca,in}$ is decreased 20%.

In order to generate a set of residual, a full-order observer is built as follows [15]:

$$\begin{cases} w(k+1) = Ew(k) + TBu(k) + Ky(k) \\ \hat{x}(k) = w(k) + Hy(k) \end{cases} \quad (62)$$

where $\hat{x}$ is the estimated state vector and w is the state of full-order observer. E, T, K and H are matrices to be designed for achieving unknown input decoupling requirements. The design of E, T, K and H is achieved by solving the following equations:

$$(HC - I)F_d = 0 \quad (63a)$$

$$T = I - HC \quad (63b)$$

$$E = A - HAC - K_1C \quad (63c)$$

$$K_2 = EH \quad (63d)$$

$$K = K_1 + K_2 \quad (63e)$$

If the following conditions are fulfilled: (1) $Rank(CF_d) = Rank(F_d)$, (2) (C, A_1) is a detectable pair, where $A_1 = E + K_1C$, an unknown input observer provides an estimation of the state vector, used to generate a residual vector:
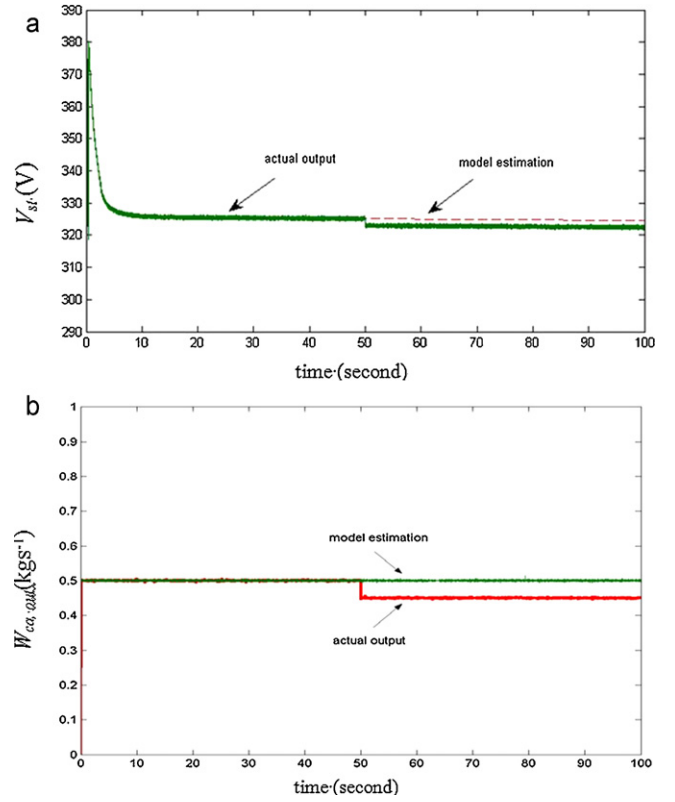
$$r(k) = y(k) - C\hat{x}(k) \quad (64)$$

Fig. 5. Comparison of actual output and model estimation when $W_{ca,in}$ is decreased 10%.

4. Results and discussion

The research results apply to hybrid power sources bus which includes fuel cell, PV and lithium-ion battery. In this hybrid power sources bus the maximal power of fuel cell is 75 kW, the maximal power of PV is 1.5 kW and the capacity of lithium-ion battery is about 15 Ah. The proposed model-based fault diagnosis method is implemented in Matlab/Simulink environment. Results of three of the proposed fault scenarios (f1, f2 and f3) are presented. f1, f2 and f3 are increase in the compressor motor's friction, humidifier choking and decrease in total absorbed irradiance of the PV system, respectively. According to Eq. (64), r_1, r_2, r_3, r_4 are the residuals of $[V_{st}, W_{ca,out}, I_{pv}, i_b]$.

As discussed in previous sections, the fault detection is based on checking the difference (residual) between the signals monitored by a sensor and its estimation using the detection model at each sample time. The fault f1 (increase in the compressor motor's friction) is introduced into the system at time 50 s creating changes in its internal dynamics. When the compressor motor's friction increase, the mass flow rate of air entering the cathode ($W_{ca,in}$) is decrease 20%, the actual output and model estimation of V_{st}, $W_{ca,out}$ are shown in Fig. 3(a) and (b). The residuals r_3, r_4 are almost zero and the residuals r_1, r_2 are shown in Fig. 4(a) and (b). Threshold of V_{st} (dash line in Fig. 4(a)) is about ±3 V and threshold of $W_{ca,out}$ (dash line in Fig. 4(b) is about ±0.1 kg s⁻¹). Fig. 4(a) and (b) shows that the residuals r_1, r_2 are larger than their threshold after 50 s. So the residuals r_1, r_2 are sensitive to f1 and the residuals r_3, r_4 are not sensitive to f1. Then we can detect the f1 by calculating the residuals r_1 and r_2. When the compressor motor's friction increase, the mass flow rate of air entering the cathode ($W_{ca,in}$) is decrease 10%, the actual output and model estimation of V_{st}, $W_{ca,out}$ are shown in Fig. 5(a) and (b). The residuals r_3, r_4 are almost zero and the residuals r_1, r_2 are shown in Fig. 6(a) and (b). Fig. 6(a) and (b) shows that the residuals r_1, r_2 are smaller than their threshold after 50 s
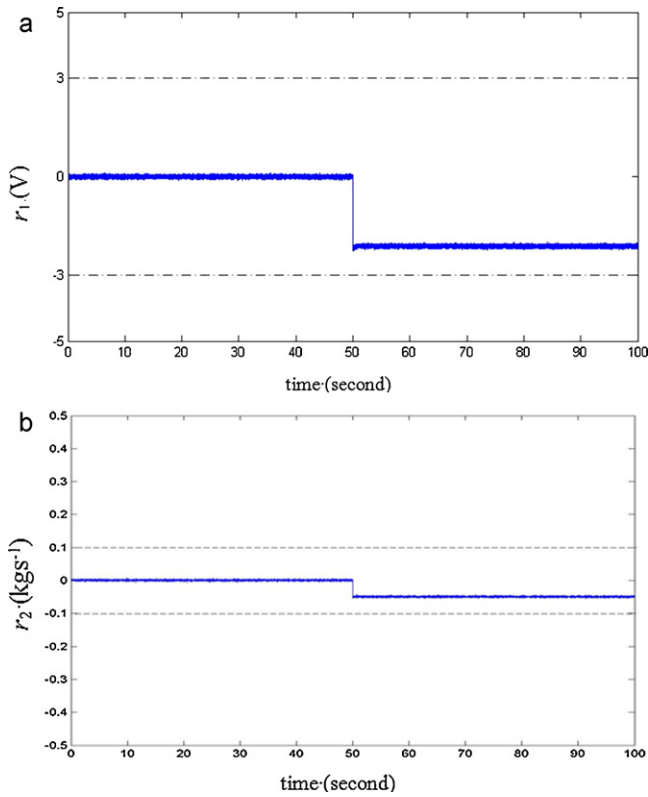
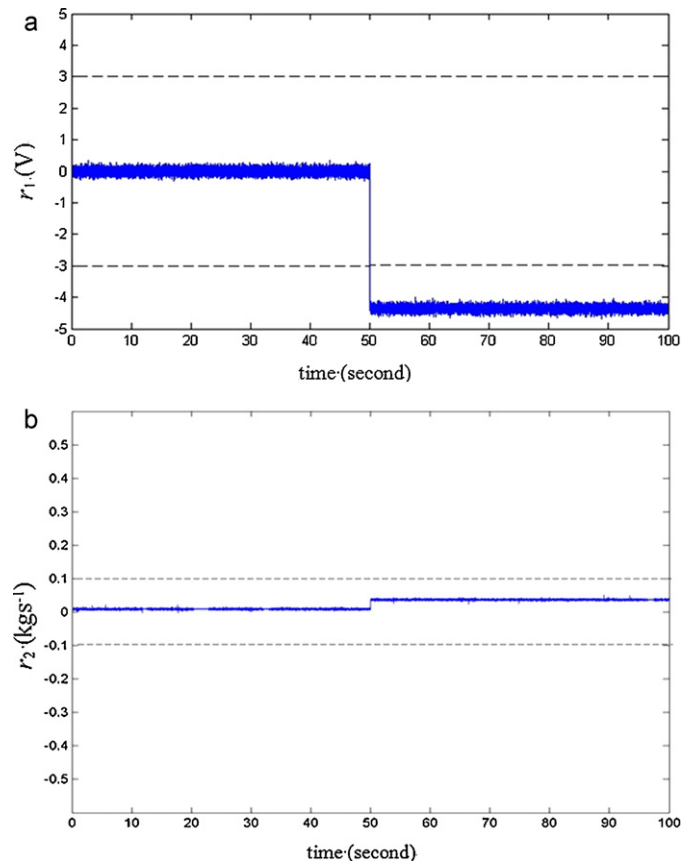**Fig. 6.** Time evolution of the residual when $W_{ca,in}$ is decreased 10%.

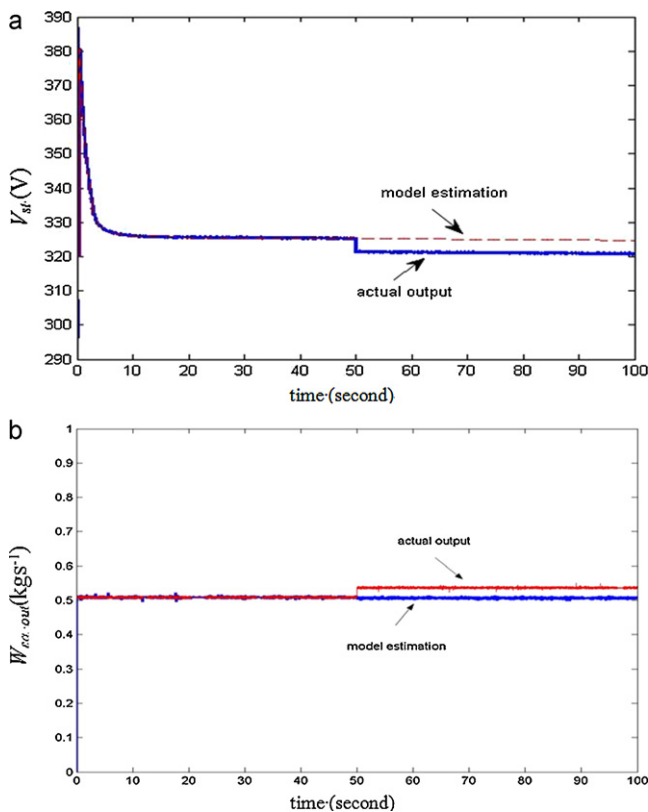**Fig. 8.** Time evolution of the residual corresponding to fault $f2$.

Fig. 7. Comparison of actual output and model estimation when $f2$.

and the fault $f1$ is not detected. So the result of fault detection is sensitive to the magnitude of fault.

The fault $f2$ is the choking of humidifier. The fault $f2$ is introduced into the system at time 50 s creating changes in its internal dynamics. When the fault $f2$ is applied, the actual output and model estimation of V_{st}, $W_{ca,out}$ are shown in Fig. 7(a) and (b). The residuals r_3, r_4 are almost zero and the residuals r_1, r_2 are shown in Fig. 8(a) and (b). Fig. 8(a) and (b) shows that the residual r_1 is larger than the threshold and r_2 is less than the threshold after 50 s. This shows that fault $f3$ appear. So the residual r_1 is sensitive to $f2$ and the residuals r_2, r_3, r_4 are not sensitive to $f2$. Then we can detect the $f2$ by calculating the residuals r_2.

The fault $f3$ is decrease in total absorbed irradiance of the PV system. The fault $f3$ is introduced into the system at time 50 s creating
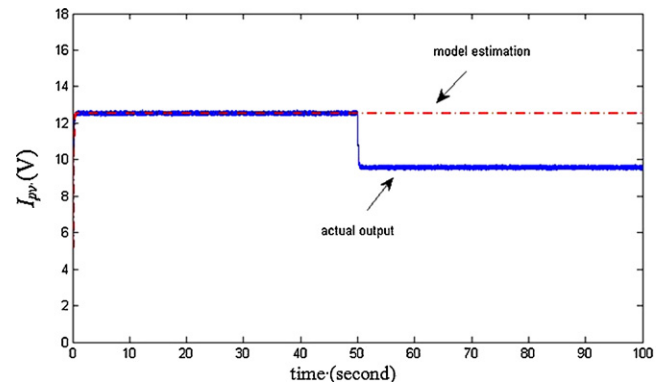

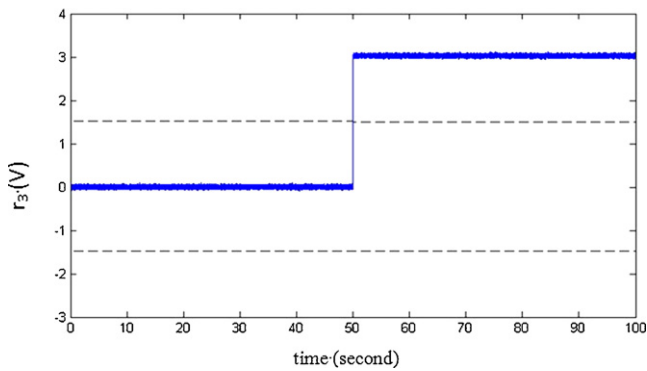**Fig. 9.** Comparison of actual output and model estimation corresponding to fault $f3$.

Fig. 10. Time evolution of the residual corresponding to fault $f3$.

changes in its internal dynamics. When the fault $f3$ is applied, the actual output and model estimation of I_{pv} are shown in Fig. 9. The residuals r_1, r_2, r_4 are almost zero and the residual r_3 is shown in Fig. 10. Threshold of I_{pv} (dash line in Fig. 10) is about ± 1.5 A. Fig. 10 shows that the residual r_3 is larger than the threshold after 50 s. This shows that fault $f3$ appear. So the residual r_3 is sensitive to $f3$ and the residuals r_1, r_2, r_4 are not sensitive to $f3$. Then we can detect the $f3$ by calculating the residuals r_3.

From the simulation results we can see that we can detect fault $f1$, $f2$ and $f3$ by calculating the corresponding residuals r_1, r_2 and r_3. This shows that the proposed model-based fault detection method can detect faults of hybrid DC power sources on-line.

5. Conclusions

In this paper, a new model-based fault detection methodology of hybrid DC power sources has been presented and tested. An advantage of this new methodology is that it can find the fault on line, improve the generation time and avoid permanent damage to the equipment. To prove this methodology, a hybrid DC power sources Matlab simulator based on the state space model is built. The simulator is modified to include a set of possible fault scenarios proposed in this work. This modified simulator allows imposing a determined fault scenario, within the considered set of faults in the hybrid DC power sources and analysis its behavior. All the simulated faults have been tested with the new fault detection methodology. The results show that the proposed model-based fault detection method can detect faults of hybrid DC power sources effectively.

References

[1] L.A.M. Riascos, M.G. Simoes, P.E. Miyagi, Journal of Power Sources 175 (1) (2008) 419–429.
[2] T. Escobet, D. Feroldi, S.D. Lira, V. Puig, J. Quevedo, J. Riera, M. Serra, Journal of Power Sources 192 (1) (2009) 216–223.
[3] S.K. Firth, K.J. Lomas, S.J. Rees, Solar Energy 84 (4) (2010) 624–635.
[4] M. Staroswiecki, G. Comtet-Varga, Automatica 37 (2001) 687–699.
[5] R.J. Patton, J. Chen, Proceedings of the 30th IEEE CDC, England, 1991, pp. 2242–2247.
[6] R. Isermann, Automatica 29 (1993) 815–835.
[7] J. Amphlett, R. Baumert, R. Mann, B. Peppley, J. Roberge, Electrochemical Society 142 (1) (1995) 9–15.
[8] J.T. Pukrushpan, A.G. Stefanopoulou, H. Peng, Control of Fuel Cell Power Systems: Principles, Model, analysis and Feedback Design, Springer-Verlag, London, 2004, pp. 31–53.
[9] J.A. Adams, W.C. Yang, K.A. Oglesby, K.D. Osborne, SAE Paper 2000-01-1061, 2000.
[10] W. De Soto, S.A. Klein, W.A. Beckman, Solar Energy 80 (2006) 78–88.
[11] L.J. Gao, S.Y. Liu, R.A. Dougal, IEEE Transactions on Components and Packaging Technologies 25 (3) (2002) 495–505.
[12] D. Bernardi, E. Pawlikowski, J. Newman, Journal of Electrochemical Society 132 (1) (1985) 5–12.
[13] H. Noura, D. Theilliol, J.C Ponsart, A. Chamseddine, Fault-tolerant Control Systems: Design and Practical Applications, Springer, London, 2009.
[14] G.H. Golub, C.F. Van Loan, Matrix Computations, second edition, The Johns Hopkins University Press, 1989.
[15] J. Chen, R.J. Patton, Robust Model-based Fault Diagnosis for Dynamic Systems, Kluwer Academic Publishers, 1999.